

# Flexocaloric effect in superelastic materials

Cite as: APL Mater. 10, 121103 (2022); <https://doi.org/10.1063/5.0129331>

Submitted: 14 October 2022 • Accepted: 16 November 2022 • Published Online: 05 December 2022

 Clàudia Pérez-Junyent,  Marcel Porta,  Emma Valdés, et al.



View Online



Export Citation



CrossMark

## ARTICLES YOU MAY BE INTERESTED IN

[Local cation order and ferrimagnetism in compositionally complex spinel ferrites](#)

APL Materials 10, 121102 (2022); <https://doi.org/10.1063/5.0123728>

[Reconfigurable self-powered deep UV photodetectors based on ultrawide bandgap ferroelectric ScAlN](#)

APL Materials 10, 121101 (2022); <https://doi.org/10.1063/5.0122943>

[Electrocaloric cooling—From materials to devices](#)

Journal of Applied Physics 132, 240901 (2022); <https://doi.org/10.1063/5.0132533>

## APL Materials

**SPECIAL TOPIC:** Phononic Crystals  
at Various Frequencies

Read Now!

# Flexocaloric effect in superelastic materials

Cite as: APL Mater. 10, 121103 (2022); doi: 10.1063/5.0129331  
Submitted: 14 October 2022 • Accepted: 16 November 2022 •  
Published Online: 5 December 2022



Clàudia Pérez-Junyent,<sup>1</sup> Marcel Porta,<sup>2,a)</sup> Emma Valdés,<sup>1</sup> Lluís Mañosa,<sup>1,a)</sup> Antoni Planes,<sup>1,a)</sup>   
Avadh Saxena,<sup>3</sup> and Eduard Vives<sup>1,b)</sup>

## AFFILIATIONS

<sup>1</sup> Departament de Física de la Matèria Condensada, Facultat de Física, Universitat de Barcelona, Martí i Franquès 1, 08028 Barcelona, Catalonia

<sup>2</sup> Departament de Física Quàntica i Astrofísica, Facultat de Física, Universitat de Barcelona, Martí i Franquès 1, 08028 Barcelona, Catalonia

<sup>3</sup> Theoretical Division, Los Alamos National Laboratory, Los Alamos, New Mexico 87545, USA

<sup>a)</sup> Also at: Institute of Nanoscience and Nanotechnology of the University of Barcelona (IN<sup>2</sup>UB), Barcelona, Catalonia.

<sup>b)</sup> Also at: University of Barcelona Institute of Complex Systems (UBICS), Barcelona, Catalonia.

Author to whom correspondence should be addressed: [eduard@fmc.ub.edu](mailto:eduard@fmc.ub.edu)

## ABSTRACT

We present a combined theoretical–experimental study of flexocaloric effects in superelastic materials exhibiting structural transitions. We study a Ginzburg–Landau model combined with a vibrational model for a beam near a ferroelastic transition loaded with a three-point bending setup. We also perform experiments on a Cu–Al–Ni single crystal undergoing a martensitic transition. We measure bent beam profiles, vertical force vs vertical deflection during a slow isothermal process, time evolution of the bending and unbending amplitudes, and the evolution of temperature profiles. We also compute the evolution of heat source and heat sink profiles. Finally, we study the location of acoustic emission events during the bending/unbending experiment. Our observations are consistent with the model predictions and allow us to identify the main physical parameters relevant for flexocaloric applications.

© 2022 Author(s). All article content, except where otherwise noted, is licensed under a Creative Commons Attribution (CC BY) license (<http://creativecommons.org/licenses/by/4.0/>). <https://doi.org/10.1063/5.0129331>

## I. INTRODUCTION

The present climatic crisis is expected to drastically intensify in the forthcoming years due to the increasing needs for refrigeration, which are rising especially in developing countries.<sup>1</sup> Present room temperature refrigeration technology is based to a large extent on compression–expansion processes of fluids within their heterogeneous region. The environmental problem is caused by the commonly used refrigerant fluids that have a very negative impact on global warming due to their high capacity for absorption of infrared (IR) radiation. In recent years, there has been a growing interest in the development of more efficient and environmentally friendly cooling technologies that would help in mitigating adverse greenhouse effects. Among the proposed solutions, it is acknowledged that mechanocaloric cooling is likely to play an important role.<sup>2,3</sup>

In general, caloric effects are defined as the reversible thermal changes that occur in a solid material in response to an external

field, either magnetic, electric or mechanical. In the case of the mechanocaloric effect, thermal changes are induced by a mechanical field. Most of the work to date has been carried out by the application and removal of uniaxial stress or hydrostatic pressure and the corresponding caloric effects are usually denoted as elastocaloric<sup>4,5</sup> and barocaloric effects, respectively. These effects may be very large when they occur in the presence of a phase transition associated with an order parameter thermodynamically conjugated to uniaxial stress or hydrostatic pressure.<sup>6</sup> In the former case, the caloric response is expected to be large in the neighborhood of ferroelastic transitions involving a change in symmetry of the unit cell, while in the latter, the transition should be accompanied by a large volume change. In addition to uniaxial stress and hydrostatic pressure, there are many more ways to apply mechanical forces that can induce a phase transition. With this idea in mind, recently, it has been theoretically suggested that the possibility of actuating with more complex mechanical fields such as bending or twisting should have a number of advantages.<sup>7</sup> These mechanical modes cause strong

strain gradients concentrated in the regions of maximum curvature. In these regions, the transition is induced with much smaller forces than those needed by application of homogeneous stresses and, therefore, these modes are worth considering with the aim of optimizing the mechanocaloric response of materials with suitable elastic properties. In addition, these results suggest that a ferroelastic transition should occur with very little hysteresis, which is the main requirement for a material to display a highly stable and reproducible caloric response during a loading-unloading cycling process.

There are a few experimental studies that seem to confirm the interest in inducing mechanocaloric effects by stress modes such as bending or twisting,<sup>8-12</sup> which are denoted as flexocaloric and twistocaloric effects, respectively. In these studies, however, the relation of the flexocaloric response and phase transition dynamics driving the induced curvature has not been studied in detail. This is an essential feature that needs to be properly understood when the aim is to transfer these materials to actual refrigeration devices. Filling this gap is the main goal of the present paper.

Specifically, the work reported here is aimed at advancing the basic science of mechanocaloric cooling with the main objective of better understanding the flexocaloric effects in a realistic driving setup. For this purpose, we will first develop a model for a three point bending experiment of a ferroelastic material exhibiting a phase transition. The model is two dimensional (2D) and corresponds to a simplified structural transition. It is simple enough to be solved by numerical simulation but contains the main physical ingredients for the understanding of the relevant phenomenon. Second, we will perform detailed experimental measurements on a Cu-Al-Ni single crystal that is known to display very good elastocaloric properties. This material undergoes a ferroelastic/martensitic transition from a high temperature cubic phase to a low temperature monoclinic phase. Associated with the transition, this material shows shape memory and superelastic properties.<sup>13</sup> Superelasticity means that huge deformations, which can be even larger than 10%, associated with the stress induced transition can be recovered with very small hysteresis upon unloading. This property is, in fact, at the origin of excellent elastocaloric properties displayed by these materials. The fact that this superelastic property also occurs by bending suggests that this class of materials should also show interesting flexocaloric effects.

The influence of the transition dynamics on flexocaloric properties will be studied by combining macroscopic mechanical measurements with infrared and acoustic emission (AE) detection. Infrared imaging is a suitable experimental approach that provides localized thermal information at mesoscopic scales enabling the detection of thermal sources. Acoustic emission allows us to obtain mechanical information at microscopic scales and with high temporal resolution. The simultaneous use of several AE transducers is very useful for the detection and location of intermittency effects during bending and unbending processes.<sup>14-16</sup>

## II. MODEL

We use a mesoscopic model for a ferroelastic material exhibiting a square-to-rectangle phase transition that can be induced by either a temperature change or an applied stress. This ferroelastic material will be the constituent of a 2D macroscopic beam with free

boundary conditions. This is a drastic simplification of the phase transition occurring in the material used in the experimental part of this paper. However, the existence of a structural phase transition that can be induced by bending is the essential feature that will give us insight into the caloric response of the beam from a qualitative point of view.

The model is based on that presented in Ref. 7 but instead of considering a continuous distribution of applied forces, it mimics the present three-point bending conditions. Its main features are summarized as follows. The Helmholtz free energy of a three-dimensional (3D) beam is written as the free energy of a set of  $3N$  classical harmonic oscillators, which are the building blocks of the beam,

$$\mathcal{F}_{vib} = k_B T \sum_{i=1}^{3N} \ln \left( \frac{\hbar \omega_i}{k_B T} \right), \quad (1)$$

where  $k_B$  is the Boltzmann constant,  $T$  is the temperature,  $\hbar$  is the reduced Planck constant, and  $\omega_i$  is the angular frequency of the  $i$ -th oscillator. This free energy is divided into two terms,

$$\mathcal{F}_{vib} = \mathcal{F}_\omega + \mathcal{F}_T, \quad (2)$$

the first term,  $\mathcal{F}_\omega$ , containing the dependence of vibrational free energy on the frequencies of the oscillators, and the second term,  $\mathcal{F}_T$ , which only depends on temperature,

$$\begin{aligned} \mathcal{F}_\omega &= k_B T \sum_{i=1}^{3N} \ln \left( \frac{\hbar \omega_i}{U} \right), \\ \mathcal{F}_T &= -3N k_B T \ln \left( \frac{k_B T}{U} \right), \end{aligned} \quad (3)$$

where  $U$  is the reduced unit of energy. Assuming that the beam has no boundaries in the third dimension and that all physical quantities are constant along this direction, the free energy term  $\mathcal{F}_\omega$  is written as a functional of the 2D mesoscopic strain fields,  $e_m$ , and the 2D strain gradients,  $\partial e_m / \partial X_i$ , of the beam,

$$\mathcal{F}_\omega = \int f_\omega(e_m, \partial e_m / \partial X_i) d\mathbf{X}, \quad (4)$$

where  $X_i$  is the  $i$ -th component of the position vector of a volume element of the beam in the undistorted configuration. The free energy density  $f_\omega$  is modeled using a Ginzburg-Landau expansion,

$$\begin{aligned} f_\omega &= \frac{1}{2} \alpha (T - T_c) e_2^2 + \frac{1}{4} \beta e_2^4 + \frac{1}{6} \gamma e_2^6 + \frac{1}{2} A_1 e_1^2 \\ &+ \frac{1}{2} A_3 e_3^2 + \frac{1}{2} \kappa_1 |\nabla e_1|^2 + \frac{1}{2} \kappa_2 |\nabla e_2|^2 + \frac{1}{2} \kappa_3 |\nabla e_3|^2, \end{aligned} \quad (5)$$

where  $\alpha$ ,  $\beta$ ,  $\gamma$ ,  $A_1$ ,  $A_3$ ,  $\kappa_1$ ,  $\kappa_2$ , and  $\kappa_3$  are parameters,  $T_c$  is a temperature characterizing the stability limit of the square phase and  $e_1 = (\varepsilon_{xx} + \varepsilon_{yy})/\sqrt{2}$ ,  $e_2 = (\varepsilon_{xx} - \varepsilon_{yy})/\sqrt{2}$  and  $e_3 = \varepsilon_{xy}$  are the symmetry adapted strains, which are written in terms of the components of the Lagrangian strain tensor,  $\varepsilon_{ij}$ .

The dynamical equation of the displacement,  $\mathbf{u}$ , of a volume element of the beam can be written as

$$\rho_0 \ddot{u}_i = \rho_0 g_i + \sum_j \frac{\partial \tau_{ij}}{\partial X_j}, \quad (6)$$

where the dots stand for time derivative,  $\rho_0$  is the density of the undistorted beam,  $g_i$  is the  $i$ -th component of an external force (per unit mass), and  $\tau_{ij}$  are the components of the first Piola–Kirchhoff stress tensor.<sup>17</sup> The first Piola–Kirchhoff stress tensor is the work conjugate of the deformation gradient,  $F_{ij}$ , which is defined as

$$F_{ij} = \frac{\partial u_i}{\partial X_j} + \delta_{ij}, \quad (7)$$

where  $\delta_{ij}$  is the Kronecker delta. Thus, using the chain rule, the first Piola–Kirchhoff stress tensor can be obtained from the Helmholtz free energy as

$$\tau_{ij} = \frac{\delta \mathcal{F}_{vib}}{\delta F_{ij}} = \sum_{m=1}^3 \frac{\delta \mathcal{F}_\omega}{\delta e_m} \frac{\partial e_m}{\partial F_{ij}}. \quad (8)$$

A damping force derived from a Rayleigh potential is also included to dissipate the excess free energy during relaxation.

To be able to compare simulations to experiments, in the present work, the external forces are applied to three points of the beam only, as shown schematically in Fig. 1. At equilibrium, the three forces must satisfy

$$\sum_{n=1}^3 \mathbf{f}_n = 0, \quad (9)$$

$$\sum_{n=1}^3 (x_n f_{ny} - y_n f_{nx}) = 0,$$

where  $\mathbf{f}_n$  is the  $n$ -th force and  $x_n$  and  $y_n$  are the Cartesian coordinates of the point where the  $n$ -th force is applied. The components  $x_n$  are fixed throughout the bending process with  $x_3 - x_1 = x_1 - x_2 = \Delta$ . Moreover, it is assumed that the forces  $\mathbf{f}_2$  and  $\mathbf{f}_3$  are perpendicular to the longitudinal axis of the beam. Applying these constraints, all forces are written in terms of  $f_{2x}$ , which becomes the control parameter,

$$f_2 = \frac{f_{2x}}{\sin(\theta_2)},$$

$$f_3 = \frac{\Delta \cos(\theta_2) + (y_1 - y_2) \sin(\theta_2)}{\Delta \cos(\theta_3) + (y_1 - y_3) \sin(\theta_3)} f_2, \quad (10)$$

$$f_{1x} = -f_2 \sin(\theta_2) + f_3 \sin(\theta_3),$$

$$f_{1y} = f_2 \cos(\theta_2) + f_3 \cos(\theta_3),$$

where  $\theta_2$ ,  $\theta_3$ ,  $y_1$ ,  $y_2$ , and  $y_3$  are obtained from the current configuration of the beam. We note that if  $f_{2x} \neq -f_{3x}$ , the force  $\mathbf{f}_1$  may not be

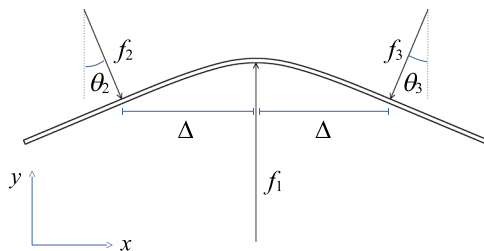


FIG. 1. Schematic representation of the beam with three applied forces.

perpendicular to the longitudinal axis of the beam (a small friction is required to satisfy these conditions).

Given a value of  $f_{2x}$ , we use Eq. (10) to determine the remaining forces. This ensures the existence of an equilibrium configuration. However, as the beam is not rigid, when these three forces are applied, the beam is not in equilibrium yet. Thus, its dynamical evolution, including energy dissipation, is simulated until a final equilibrium configuration is reached.

Application of the external forces above the transition temperature in the absence of stress results in internal stresses that induce the phase transition to the rectangular phase. The associated entropy change in isothermal conditions is

$$\Delta S = S(f_{2x}, T) - S(f_{2x} = 0, T) = -\frac{\partial \mathcal{F}_{vib}(f_{2x}, T)}{\partial T} = -\frac{\alpha}{2} \int e_2^2 d\mathbf{X}, \quad (11)$$

which is always negative. Thus, the model is appropriate to study the conventional flexocaloric effect.

The parameters  $\alpha$ ,  $T_c$ ,  $\kappa_2$ , and  $\rho_0$  are set to unity, which define reduced units of length, mass, energy, and temperature. The values of the remaining model parameters are the same as in Ref. 7, which correspond to a cubic-to-tetragonal ferroelastic transition and are adequate for our 2D model.<sup>18</sup>

The size of the simulated beam (in reduced units of length) is  $L \times w = 6875 \times 62.5$ , which is discretized onto a mesh of size  $3520 \times 32$ . Finally, all results correspond to the temperature  $T = 1.05T_c$ , which is above the ferroelastic transition temperature in the absence of stress,  $T_{tr} = T_c + 3\beta^2/16\alpha\gamma = 1.029T_c$ .

### III. EXPERIMENTAL DETAILS

#### A. Sample

The studied sample is a superelastic single crystal with nominal composition  $\text{Cu}_{67.7}\text{Al}_{26.7}\text{Ni}_{5.6}$  at. %, produced by Nimesis Technology (France). The sample dimensions are  $110 \times 5 \times 1 \text{ mm}^3$ . By x-ray diffraction experiments, we have confirmed that the long symmetry axis is oriented along the  $\langle 100 \rangle$  crystallographic direction of the cubic phase, as stated by the manufacturer. The sample transforms from the cubic phase to an 18R martensitic phase (monoclinic).

Calorimetric measurements at zero stress [see Fig. 2(a)] on a small piece ( $m = 33.60 \text{ mg}$ ) cut from the sample reveal that the transition starts, when cooling, at  $M_s = 258 \pm 1 \text{ K}$ , and extends to more than 57 K. When heating, there is a hysteresis of  $\sim 10\text{--}12 \text{ K}$ . By integrating the calorimetric curves, one can obtain the latent heat of the transition,  $\Delta H = 5.4 \pm 0.2 \text{ J/g}$ . The error bar includes the values for both heating and cooling runs. Figure 2(b) shows the stress–strain hysteresis loop when applying uniaxial tensile stress, at room temperature, at 2 mm/min. The stress is estimated assuming a constant cross-section, and the strain is the elongation divided by the original length. The transition starts at  $\sigma_T = 90 \pm 5 \text{ MPa}$  and the stress hysteresis, when unloading, is  $\sim 25 \text{ MPa}$ .

#### B. Mechanical test

Figure 3 shows a schematic representation of the experimental setup that consists of an inverted three point bending experiment.

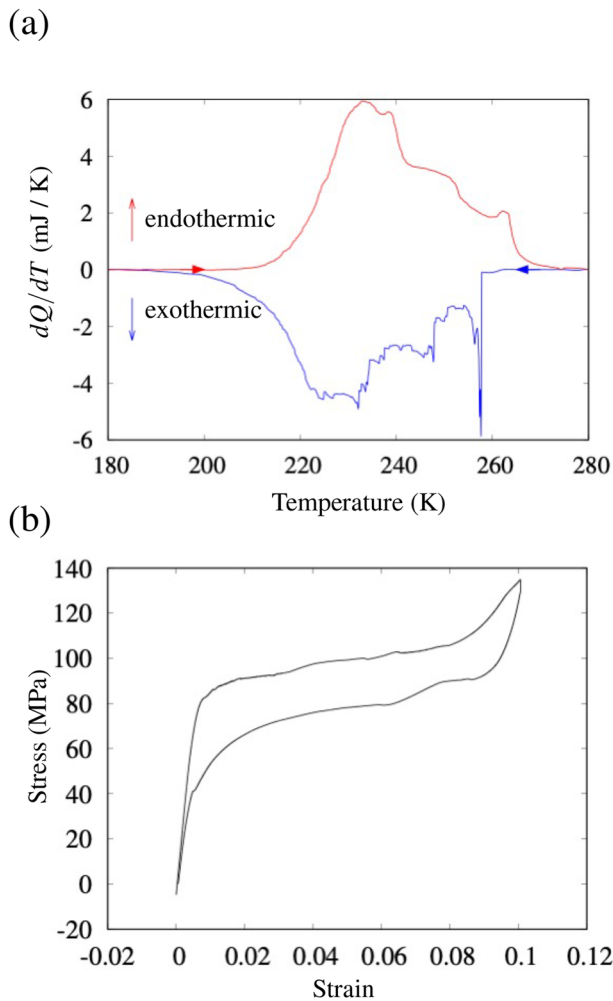


**FIG. 2.** (a) Calorimetric curves obtained by heating and cooling ramps of a small piece of the studied Cu–Al–Ni sample. The upper red curve corresponds to a heating run (martensite–austenite, endothermic) and the lower blue curve to a cooling run (austenite–martensite, exothermic). (b) Stress–strain loop at room temperature under uniaxial tensile loading and unloading along the long axis of the sample.

The moving frame is controlled by a Zwick/Roell Z005 5 kN materials testing machine. This frame allows for the vertical displacement of the two upper pins (separated by a distance  $2\Delta = 60$  mm). These are in contact with the upper face of the sample, which sits centered on the static central pin. The load cell, placed on top of the frame, measures the vertical force with a resolution of 0.5 N. The vertical displacement of the frame is controlled with a resolution of 0.1 mm. Experiments at different vertical velocities have been performed in the range 1 mm/min (almost isothermal conditions) to 2000 mm/min (i.e., fast adiabatic conditions).

The pins are made of steel, but the central lower pin, when required to improve adiabatic conditions, can be replaced by a plastic one in order to avoid, as much as possible, heat losses in the region imaged by the IR camera.

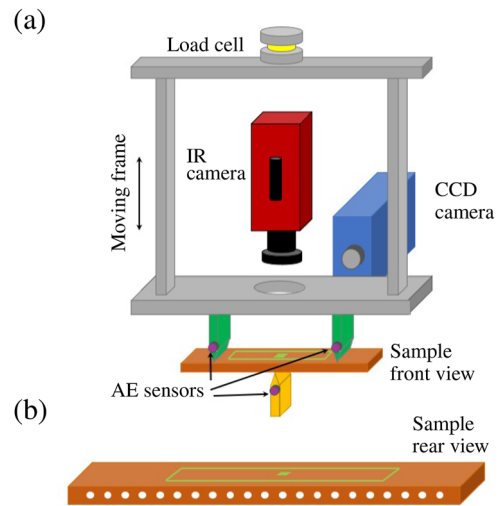


**FIG. 3.** (a) Schematic of the inverted three points bending experiment for the study of flexocaloric effects. The sample (brown) is sitting on the lower pin (orange) and is bent by the upper pins (green). The diagram also shows the position of the infrared camera that records images of the central part of the sample surface and the optical CCD camera recording its rear edge. The load cell, in the upper part of the frame (yellow), measures the applied vertical force. Acoustic emission sensors (violet) are placed on the three pins used for bending. (b) Back view of the sample showing the 21 white dots (spaced 5 mm) used for the digitization of the sample profiles. The green square on the sample surface indicates (schematically) the  $20 \times 20$  pixel region where the average central temperature is measured, and the long green rectangle indicates the region ( $625 \times 50$  pixels) used for the determination of 1D temperature profiles.

We emphasize that the control parameter is the vertical displacement of the frame, which is equal to the vertical deflection of the beam,  $\Delta y$ . This is in contrast to the simulations, where the control parameter is the horizontal force applied to the beam.

A CCD optical camera working at 5 fps is placed at the rear of the setup allowing for video recording of the lateral edge of the sample, which displays 21 small white dots that, after a proper digitization, allow for a precise measurement of the sample profile during the bending experiment.

### C. IR measurements

An infrared camera Infratec8800 is placed in a fixed position inside the moving frame. By a convenient hole in the moving frame, we can obtain images of the central position of the sample at a frequency of 600 fps. Given this configuration, the distance from the IR camera to the sample surface is approximately constant. This allows us to reach good focusing conditions during the whole experiment. The spatial resolution is 18.3 pixel/mm and the temperature resolution is 35 mK.

In order to improve the accuracy of the temperature measurements, the upper surface of the sample is covered with high emissivity and low reflectivity black matt paint, which avoids reflections of IR radiation. The full setup is surrounded with a polystyrene shield ensuring a good homogeneous thermal environment.

By proper numerical processing of the IR camera maps, it is possible to derive the following information on the surface sample

temperature. First, the average central temperature  $T_0(t)$  is defined as the average temperature over a square of  $20 \times 20$  pixels centered on the sample [see Fig. 3(b)]. Second, temperature profiles along the sample length  $T(x, t)$  are obtained by averaging the temperature readings along 50 pixels centered on the sample width.

Assuming that there are no heat losses, the evolution of the 1D profiles  $T(x, t)$  will obey the Fourier equation that can be expressed as

$$C\rho \frac{\partial T(x, t)}{\partial t} = \kappa \frac{\partial^2 T(x, t)}{\partial x^2} + \sigma(x, t), \quad (12)$$

where  $C$  is the heat capacity per unit mass,  $\rho$  is the density, and  $\kappa$  is the thermal conductivity. These three parameters are considered to be constant. We have used the following values, obtained from the literature:<sup>19</sup>  $\rho = 7120 \text{ kg m}^{-3}$ ,  $C = 450 \text{ J K}^{-1} \text{ kg}^{-1}$ , and  $\kappa = 45 \text{ W m}^{-1} \text{ K}^{-1}$ . The term  $\sigma(x, t)$  accounts for the heat production (energy per unit time and per unit volume) due to the moving transformation fronts that will emit or absorb latent heat.

By a careful numerical analysis (as explained in Ref. 20), this equation can be inverted in order to obtain the evolution of the heat sinks and sources, defined as

$$\Sigma(x, t) \equiv \frac{\sigma(x, t)}{C\rho}. \quad (13)$$

Note that  $\Sigma$  is defined as the temperature change per unit time, and is positive when there is heat production (forward austenite–martensite transition) and negative when there is heat absorption (reverse martensite–austenite transition).

Note also that the integration of  $\sigma(x, t)$  in a chosen central region of the sample, for instance, between  $(-x_0, x_0)$ , during the whole duration of the transition ( $t_{ini} - t_{fin}$ ) will allow an estimation of the total heat emitted or absorbed ( $Q$ ) due to the phase transformation,

$$Q = A \int_{-x_0}^{x_0} dx \int_{t_{ini}}^{t_{fin}} dt \sigma(x, t), \quad (14)$$

where  $A$  is the sample cross-section. When  $Q$  is compared to the latent heat of the transformation, it is possible to estimate the transformed fraction  $\chi$  in the selected region as

$$\chi = \frac{Q}{2x_0 A \Delta H}. \quad (15)$$

#### D. AE measurements

In order to investigate the intermittent avalanche dynamics of the martensitic transition, three acoustic emission (AE) sensors (micro-80, from Europhysical Acoustics) working in the ultrasonic range 200 kHz–1 MHz are placed on the bending pins. A thin vase-line film is placed between the transducers and the pins as well as between the sample and the pins in order to ensure good ultrasound transmission.

AE signals from the sensors are preamplified (60 dB) and input into two two-channel PCI-2 acquisition cards from the Mistras group working at 40 MHz. Individual AE hits were defined in every channel in the following way: a hit starts at time  $t_{ini}$  when the absolute value of the preamplified signal  $|V(t)|$  crosses a noise

threshold (25 dB, equivalent to 17.78 mV) and ends at  $t_{final}$  when  $|V(t)|$  remains below the threshold for more than 100  $\mu\text{s}$ . The energy of a hit is given by  $E = \frac{1}{10k\Omega} \int_{t_{ini}}^{t_{final}} (V(t))^2 dt$ .

After the measurements, the recorded hit list from the three sensors is analyzed for the 1D-location of individual AE events,<sup>21</sup> defined from any pair of consecutive hits detected in different neighbor channels (left and central, and central and right) within less than  $t_{max} = 29.1 \text{ ms}$  (this corresponds to a sound velocity of 1030 mm/s). The event location is given by  $x = 0.5\Delta \left(1 - \frac{\Delta t}{t_{max}}\right)$ , where  $\Delta = 30 \text{ mm}$  (the distance between the central pin and the two upper pins) and  $\Delta t$  is the delay between the two hits. The source energy of a located event is estimated as  $E_0 = \sqrt{E_1 E_2}$ , where  $E_1$  and  $E_2$  are the energies measured in the two neighboring channels. This formula approximately corrects for the effects of attenuation in the sample, assuming a constant exponential damping factor.

## IV. RESULTS

### A. Simulation results

In this subsection, we report the configurations of the bent beam obtained from the simulations, and the results of their elastic and caloric response.

Application of the three forces increases the deviatoric stress in the beam, especially at its central part, where the force  $f_1$  is applied. The stress is positive at the external part of the curved regions of the beam and negative at the internal part of these regions. Thus, for sufficiently large forces, different variants of the rectangular phase nucleate at opposite sides of the beam. This yields a rather heterogeneous microstructure at the central part of the beam, where several variants of the martensite phase coexist with the austenite phase. Consequently, the transformed fraction,  $\chi$ , in this region of the beam is less than one. For small forces, we obtain  $\chi \approx 0.5$ . In addition, this microstructure is separated from the untransformed regions of the beam by two fronts. The deviatoric strain field for several values of the applied forces is shown in Fig. 4(a) using a color scale.

Specifically, we plot the deviatoric strain of the beam using a red-blue scale and show in white color the regions of the beam that remain unstrained. Increasing the applied forces increases the area where the heterogeneous strain microstructure is stable, which involves the displacement of the fronts separating this microstructure from the untransformed square phase. This result is shown in a more quantitative way in Fig. 4(b) where we plot the strain vs the spatial coordinate  $x$  in the upper and lower parts of the beam for the five values of the applied forces used in Fig. 4(a).

The nucleation of the microstructure occurs at about  $f_{2x} \approx 1.03 \times 10^{-5}$ . The region where the rectangular phase is stable is clearly identified. Increasing the external forces slightly increases the strain within the rectangular phase and mainly leads to the displacement of the fronts separating the heterogeneous microstructure from the almost homogeneous square phase. It is also clear that the beam is only strained between the points where the forces  $f_2$  and  $f_3$  are applied (at  $x/2\Delta = \pm 0.5$ ). The elastic response of the beam along a bending process is shown in Fig. 4(c) where we plot the summation of the vertical components of the applied forces  $f_2$  and  $f_3$  vs the vertical displacement of the beam at the points where these forces are applied. That is, the vertical deflection of the beam,  $\Delta y \equiv \Delta(y_2 - y_1) \approx \Delta(y_3 - y_1)$ . After an initial purely elastic response,

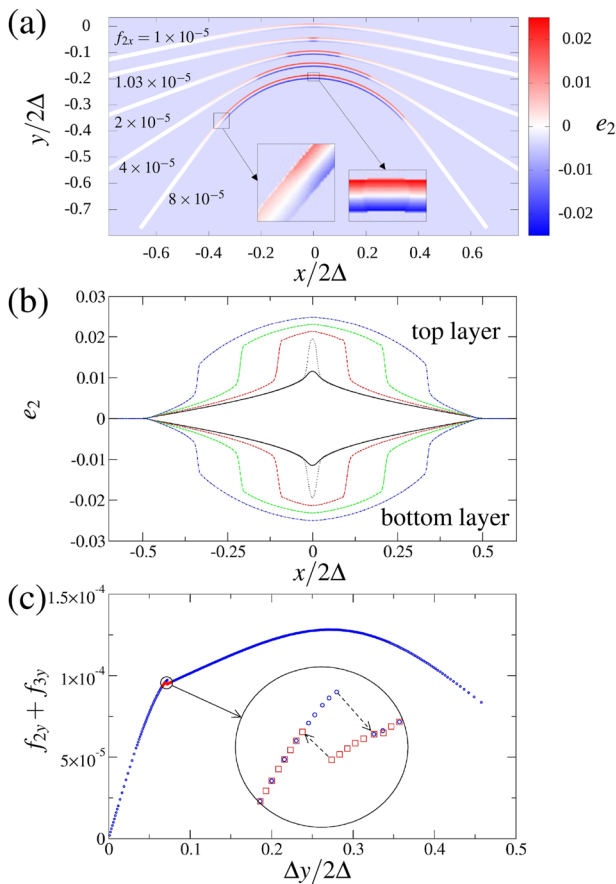


**FIG. 4.** (a) Deviatoric strain of the bent beam for five different values of the applied forces as indicated. The nucleation of two different variants of the rectangular phase upon bending and the displacement of the front separating the heterogeneous strain microstructure from the square phase are clearly visible. (b) Deviatoric strain of the bent beam along the spatial coordinate  $x$  in the top and bottom layers of the beam, where different variants of the rectangular phase nucleate. The applied forces are the same as in (a). (c) Vertical force applied to the beam vs amplitude of the vertical displacement.

the rectangular phase nucleates leading to a superelastic response. For large vertical displacements, the vertical components of the applied forces  $f_2$  and  $f_3$  decrease as their main component is horizontal. The unbending curve has been found to be identical to the bending one except in the vicinity of the nucleation of the rectangular phase, as shown in the inset of Fig. 4(c). Thus, the current simplified model yields the hysteresis associated with the nucleation of the rectangular phase only. Once this phase has been nucleated, the displacement of the interface separating the heterogeneous microstructure from the square phase occurs without hysteresis. This is in contrast to what occurs in ferroelastic materials as discussed below.

We also evaluate the local entropy of the bent beam with respect to the unstrained square phase at the same temperature as

$$s - s(f_{2x} = 0) = -\frac{\partial f_\omega}{\partial T} = -\frac{\alpha}{2} e_2^2. \quad (16)$$

This quantity is plotted in Fig. 5(a) along the spatial coordinate  $x$  vs the vertical deflection of the beam,  $\Delta y$ , using a color scale. The results shown are an average along the material coordinate  $X_y$  of the beam.

According to the results shown in Fig. 4(c), the response of the beam to small forces is purely elastic, which yields a tiny entropy change. However, at about  $\Delta y/2\Delta = 0.072$ , the nucleation of the rectangular phase occurs at the central part of the beam leading to a substantial entropy change associated with the first order character of the phase transition. As the applied force increases, the front separating the heterogeneous strain microstructure from the almost homogeneous square phase moves toward the points where the forces  $f_2$  and  $f_3$  are applied, and the length of the region where the heterogeneous microstructure is stable increases. It is worth noting that for each value of the vertical deflection,  $\Delta y$ , this entropy change (multiplied by temperature) represents the heat emitted by the beam since the beginning of the bending process. To obtain the rate of heat emitted by the beam along the bending process, in Fig. 5(b), we plot the entropy change along the spatial coordinate  $x$  per unit of vertical deflection,  $\partial s/\partial \Delta y$ , vs the vertical deflection of the beam,  $\Delta y$ . Clearly,

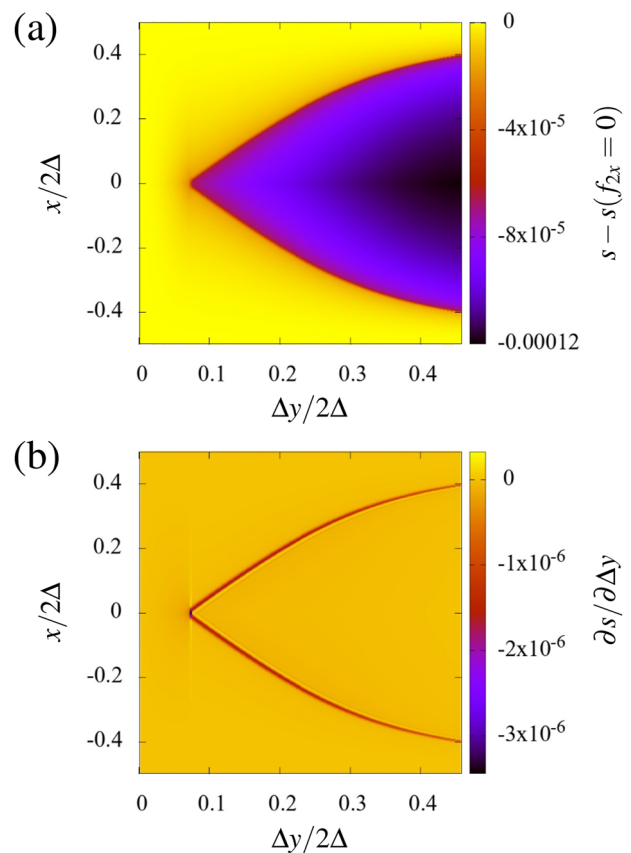


**FIG. 5.** (a) Local entropy of the beam along the spatial coordinate  $x$  vs the amplitude of the vertical displacement  $\Delta y$ . The results are averaged along the material coordinate  $X_y$ . (b) Local entropy change per unit of vertical displacement,  $\partial s/\partial \Delta y$ . The result is given along the spatial coordinate  $x$  vs the amplitude of the vertical displacement  $\Delta y$ .

the main instantaneous heat source is located at the front separating the heterogeneous microstructure from the square phase.

## B. Experimental results

### 1. Mechanical response

Figure 6(a) shows the digitized profile of the sample during a bending test performed at 500 mm/min and a maximum bending amplitude of 25 mm ( $\Delta y/2\Delta = 0.42$ ). As can be observed, only the central region of the sample with  $|x| < 10$  mm ( $|x|/2\Delta < 0.167$ ) is bending significantly. As seen in the simulations [Fig. 4(a)], the bent region of the beam is where the nucleation of the martensite phase has occurred. The curvature of the beam depends on the transformation strain so that the larger the strain, the larger the curvature and, consequently, the smaller the region where the martensite phase is stable.

Figure 6(b) shows two examples of hysteresis loops (vertical force vs vertical displacement) obtained at 1 mm/min up to a maximum bending amplitude of 35 mm ( $\Delta y/2\Delta = 0.58$ ). The bending speed is very low in order to ensure that the sample remains in isothermal conditions, thus avoiding temperature gradients. As can be seen, the loops display a similar behavior to those obtained in

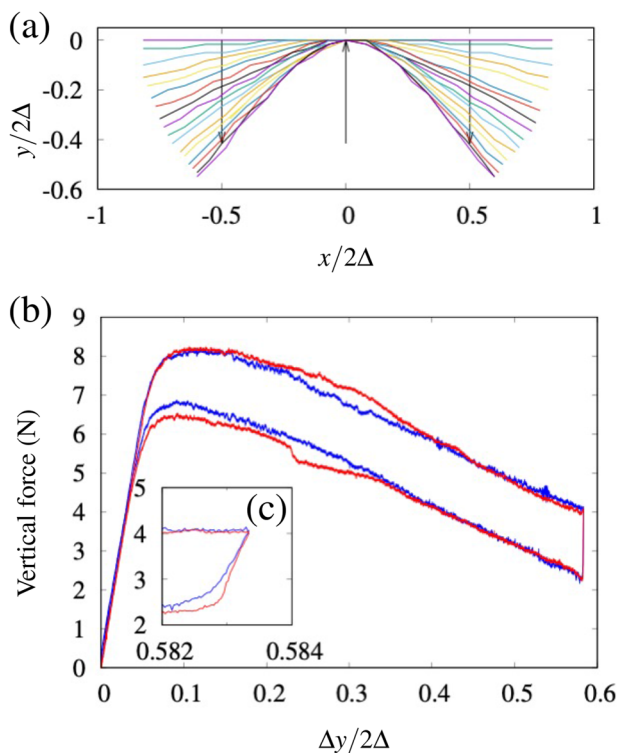


**FIG. 6.** (a) Digitized profiles of the sample at different deflections obtained during an experiment at 500 mm/min deforming until a maximum deflection of 25 mm. The profiles are separated by 0.2 s. The arrows represent the position of the bending pins. (b) Vertical force vs vertical deflection during a slow isothermal experiment at 1 mm/min down to a maximum amplitude of 35 mm. The two loops correspond to different friction coefficients between the pins and the sample surface. (c) The inset reveals the slope of the right part of the loop when the bending direction is reversed.

the simulations. The initial elastic linear part is followed by a yield point with a maximum of the force that then decreases rather linearly. After the unbending, the deformation is fully recovered. The main difference with the model is the existence of hysteresis. In the model, hysteresis is very small and only related to the nucleation of the first martensitic domains. In the experiment, we have checked that the origin of the hysteresis is not due to the friction between the pins and the sample. The two displayed loops correspond to a case in which the sample surface in contact with the upper pins is rough (due to the matt paint) and a case in which the surface is mirror polished and covered with oil. No significant difference in the hysteresis is observed, which confirms that the origin must be the internal friction of the transformation fronts due to intrinsic disorder, which is not considered in the simulations. As shown in the inset [Fig. 6(c)], one should note that the right part of the loop is not vertical but has a slope that is compatible with a behavior dominated by the elastic response of the transformed region.

### 2. Average central temperature

Figure 7 shows the evolution of the vertical displacement [(a) and (c)], the force, and the average central temperature [(b) and (d)] of the sample during a fast experiment at 2000 mm/min, down to a maximum bending amplitude of 35 mm ( $\Delta y/2\Delta = 0.5833$ ), in conditions as adiabatic as possible. Panels (a) and (b) correspond to bending and (c) and (d) to unbending. Both bending and unbending runs are carried out consecutively but separated with a waiting time of 120 s in order to allow for thermal equilibration prior to the unbending run. During bending, the central part of the sample shows an overheating of more than 3 K, which occurs after the force reaches its maximum but slightly before the bending

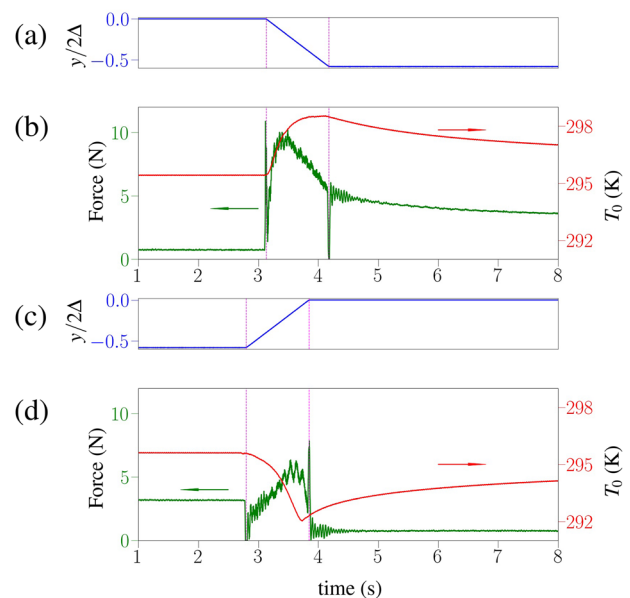


**FIG. 7.** (a) Time evolution of the bending displacement  $y/2\Delta$ . (b) The vertical force and the central temperature of the sample during a bending experiment at 2000 mm/min up to a maximum amplitude of 35 mm. (c) and (d) The same data during unbending.

run stops. When unbending, an almost symmetric undercooling is found, slightly before the sample is flat again.

Note that in these figures, the force measurement shows rather large fluctuations. This is due to the fact that the measurement is very fast and the readings from the load cell cannot be integrated enough by the electronics. Moreover, one can also observe that during the acceleration and deceleration of the materials testing machine (at the beginning and end of the linear displacement ramps), the force overshoots. The experiment is performed as fast as allowed by the electronic controller.

Although these measurements describe the overall behavior of the sample under adiabatic bending conditions and reveal the existence of a large flexocaloric effect, one must take into account that the sample temperature is not homogeneous but shows a certain time evolution and heterogeneous distribution as a consequence of the moving transformation fronts that are responsible for the heat emission or absorption (latent heat). These issues are addressed in the following subsections.

### 3. 1D thermal profiles

As explained in Sec. III C, during the experiment in adiabatic conditions with a vertical velocity of the moving frame of 2000 mm/min, we have recorded temperature maps of the sample surface at 600 fps using the IR camera. These maps are averaged over the 128

pixels corresponding to the width of the sample so that we obtain a temporal sequence of 1D temperature profiles. These are represented in Fig. 8(a) along the bending process and in Fig. 8(b) along the unbending of the beam. Temperature is represented by the color scale as indicated in the color bar located at the bottom of the figure. The vertical dashed lines represent the start and end points of the pin movement. As can be seen, during the bending run, we observe the heating of the central part of the sample followed by the thermal equilibration that is mainly due to heat conduction to the ends of the sample and the upper pins, which are beyond the observed region. In this experiment, the central pin is made of plastic in order to avoid as much as possible thermal losses in the center of the sample. A similar behavior is observed during the unbending run revealing the undercooling in the central region.

A careful observation of the contour levels in this map already reveals that the heating and cooling of the sample are not homogeneous.

### 4. Heat source and sink evolution

By means of a numerical analysis, as explained in Sec. III C, we invert the Fourier equation and obtain the evolution of the heat sinks and sources  $\Sigma(x, t)$ .

Figures 8(c) and 8(d) show the evolution of  $\Sigma$  during the bending and unbending stages of the experiment. Note that the figures

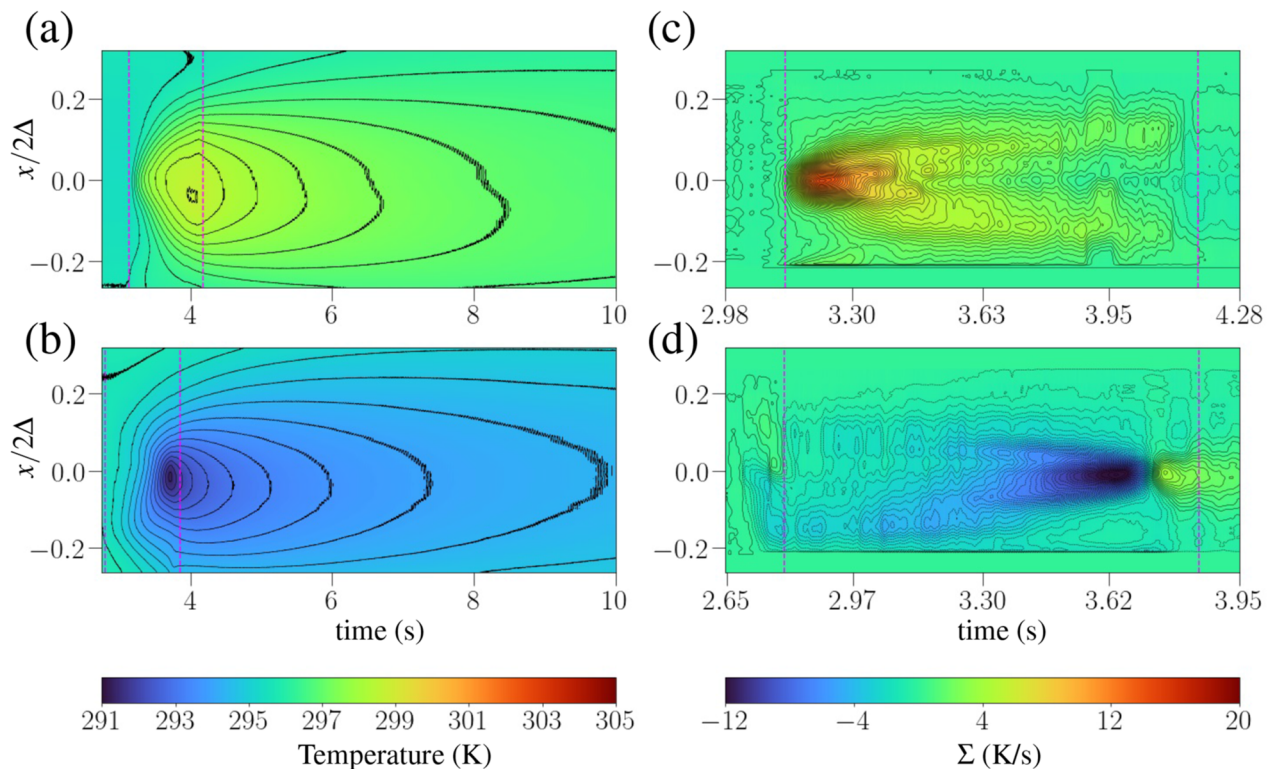


**FIG. 8.** (a) Evolution of the temperature profile along the sample as a function of time during a bending experiment at 2000 mm/min up to a maximum amplitude of 35 mm. (b) The same evolution during unbending. (c) Computed evolution of the heat source during bending, revealing the release of latent heat in two fronts moving toward the sample edges. (d) Evolution of heat sinks during unbending revealing the absorption of latent heat in two fronts moving toward the sample center.

show the temporal region of interest only, which is when the bending pins are moving. In the remaining stages of the experiment,  $\Sigma$  is essentially negligible.

As can be observed, during the bending stage, the fronts move from the center of the sample toward the right and left ends, releasing latent heat. These fronts, which correspond to the martensite phase advancing over the untransformed parent phase, reach final positions approximately at  $x = \pm 8$  mm ( $x/2\Delta = \pm 0.13$ ). During the unbending stage, the two existing fronts move back toward the center of the sample, absorbing heat, since now the parent phase in the ends of the sample advances over the central martensite region.

During bending, we observe a maximum temperature rate of  $\sim 14$  K/s near the sample center, at the beginning of the experiment, when the first martensitic domains nucleate. During unbending, a minimum heat sink of  $\sim -12$  K/s is observed near the end of the experiment (but prior to the final elastic part) when the two fronts merge in the sample center.

The trajectories of the moving fronts can be approximately located by finding the position of the maxima and minima in Figs. 8(c) and 8(d). The slope of the trajectories allows us to estimate the front velocities. These are of the order of  $\sim 8$  mm/s.

A careful observation reveals that the thermal time evolution is not smooth. The amount of heat absorbed or released per unit time is intrinsically related to the speed of the front that can be affected by existing disorder (impurities, untransformed regions, etc.) For instance, during unbending, there is a period of time in which the upper front in the picture (right front in the sample) has less cooling power, probably due to its lower velocity.

One can also remark that the cooling process stops clearly before the end of the unbending run when the sample is fully transformed to austenite and the remaining deformation is, consequently, only elastic. The observed small heat source at the center of the sample in the end of the unbending experiment [Fig. 8(d)] is an artifact caused by the heat loss in the central pin below the sample that cannot be totally avoided, despite the fact that, in this experiment, the pin is made of plastic with low thermal conductivity.

### 5. Acoustic emission avalanche response

The non-smooth evolution of the fronts is definitely evidenced by monitoring the experiment with the acoustic emission technique. The avalanche dynamics of the advancing fronts emits ultrasonic waves that propagate through the sample. In contrast to the thermal analysis, the experiments must be performed at low bending velocity in order to properly separate acoustic events that would overlap in the case of evolving at high speed.

By using three sensors, placed on the bending pins, we can detect and locate the position of the AE events as explained in Sec. III D. Figure 9 shows the position of the detected AE events as a function of time during a bending/unbending experiment at 1 mm/s with a maximum bending amplitude of 25 mm. The color indicates the source energy of the events, according to the logarithmic scale indicated in the color bar located at the right hand side of the figure. Typical error bars have been calculated by checking the difference in the position obtained from the two close sensors from the position obtained from the two distant sensors.

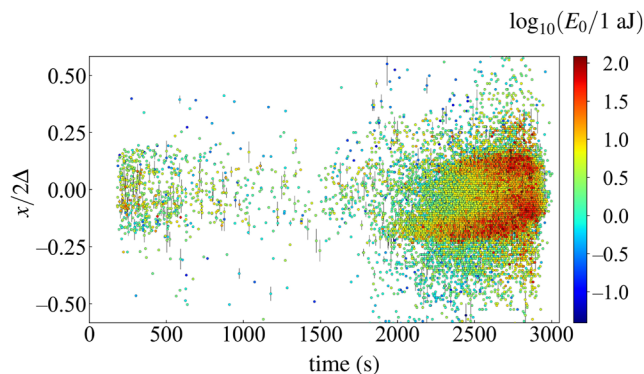


**FIG. 9.** Location of AE events during a bending/unbending experiment at 1 mm/min with a total deflection of 25 mm. There is a pause of 30 s between bending and unbending. The color scale is proportional to  $\log_{10}$  of event energy.

In the first and last 10 s of the experiment, there is almost no AE, but the force is already increasing. These two time intervals correspond to the elastic deformation of the austenite phase that does not show any AE event.

There is a clear asymmetry between the bending stage (first 1500 s) and the unbending stage (last 1500 s). The number of events in the forward transition (austenite–martensite) is 799. This is  $\sim 30$  times less than the 24 145 events located in the reverse transition (martensite–austenite). This asymmetry has already been reported in the literature when studying the thermally induced martensitic transition in Cu-based shape memory alloys.<sup>22</sup>

Due to the low AE activity in the bending run, it is difficult to reliably describe where AE signals concentrate during these runs. Instead, during unbending, it is clear that two fronts, with AE signals above 10 aJ, start at  $x/2\Delta = \pm 0.17$  ( $x = \pm 10$  mm) and move toward the center of the sample, where they merge. The two fronts are rather wide, and the observed differences with respect to the position of the sinks [Fig. 8(d)] could be due to the fact that the acoustic path is measuring the real bent distance whereas the IR camera is measuring the horizontal projection.

Note that in the end of the reverse transition, some scarce high energetic events are detected along the entire length of the sample. These might correspond to small martensitic domains that were untransformed due to pinning when the front crossed them and that suddenly transform back to the parent austenitic phase when the stress is low enough.

The energies of the located events can be estimated as explained in Sec. III D. The statistical distribution of the event energies during the unbending run is plotted in Fig. 10. The fit is performed by the maximum likelihood method and corresponds to a log-normal distribution,

$$p(E)dE = \frac{dE}{E\sigma\sqrt{2\pi}} \exp \frac{-(\ln E - \mu)^2}{2\sigma^2}, \quad (17)$$

with  $\exp(\sigma) = 2.792$  aJ and  $\exp(\mu) = 3.017$  aJ. This result is surprising since usually these distributions are expected to be power-law, as reported, for instance, for uniaxial tensile experiments in Cu–Zn–Al.<sup>23</sup>

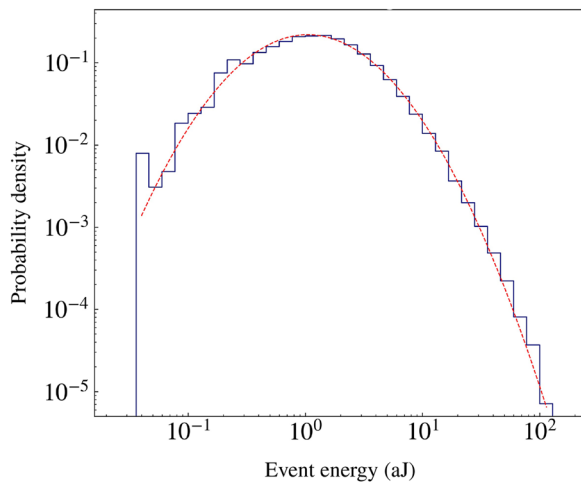


**FIG. 10.** Source energy distribution of the located AE events during the unbending run. Note that bins are logarithmic. The red dashed line corresponds to a log-normal distribution fitted by the maximum-likelihood method.

## V. DISCUSSION

From the analysis of the 2D model corresponding to a square-to-rectangle transition with two variants, we conclude that the major contribution to the flexocaloric effect is the latent heat of the transition. This heat is exchanged due to the movement of two fronts that separate an untransformed region from a partially transformed one. The microstructure in the transformed region is rather inhomogeneous and strongly restricted by the strain gradient across the beam. Consequently, in a certain region, at the end of the bending process, the transformed fraction is smaller than in a uniaxial tensile case, in which the whole sample volume is expected to transform. The model also explains why the effective forces needed to induce the transition are much smaller than in the uniaxial case, and it is suitable to describe the shape of the vertical force vs vertical displacement curve: it shows a linear elastic part, a nucleation point, a maximum and a decreasing portion. In the model, hysteresis is purely associated with the nucleation of martensite and is very weak.

Most of these features are confirmed by the experiments on Cu–Al–Ni, despite the fact that the transition is 3D from a cubic to 18R structure with 12 variants. The main discrepancy is hysteresis, which, in the experimental case, is not as weak as suggested by the model. The reason is that the movement of the fronts during bending and unbending is affected by strong pinning effects associated with disorder (dislocations, impurities, lattice incompatibilities between the variants, etc.) as revealed by the AE signals. Such a bulk disorder is not present in the model.

As explained in Sec. III C, we can get an estimation of the total transformed fraction in the central part of the sample by evaluating the total heat released or absorbed during bending and unbending. For this analysis, we choose a central 10 mm region ( $-5 \text{ mm} < x < 5 \text{ mm}$ ) that is fully crossed by the moving fronts during the bending/unbending experiment. By integrating  $\sigma(x, t)$  in this central region, along the duration of the bending/unbending stage, we obtain the total heat exchanged in this central region: during bending,  $Q = 0.595 \text{ J}$ , and during unbending,  $Q = -0.583 \text{ J}$ . The small

difference in the absolute value can be attributed to experimental errors and/or heat losses. We can compare these values with the expected latent heat obtained if the full volume of the sample in this central 10 mm region transforms. From the value of the latent heat that we have determined experimentally by calorimetric measurements ( $\Delta H = 5.2 \text{ J/g}$ ), a straightforward calculation renders  $Q_{\text{max}} = 1.92 \text{ J}$ . By comparing the values of  $Q$  and  $Q_{\text{max}}$ , we can deduce that the transformed fraction in the central region is approximately  $\chi \approx 0.3$ . This value is smaller than the transformed fraction obtained in the simulations,  $\chi \approx 0.5$ . The reason for this discrepancy is due to the fact that in a system with a larger number of variants, one expects a more complex strain microstructure giving rise to more intervariant untransformed regions. This low transformation fraction is, in principle, a drawback for the flexocaloric application. However, as important as the total heat exchanged, one should also take into account the kinetics of the transition that will finally determine the heating/cooling power.

The obtained values of the cooling power in the present flexocaloric experiments can be compared with previous elastocaloric experiments performed in Cu–Al–Ni samples with a similar composition under uniaxial stress.<sup>20</sup> In that case, by unloading the sample at  $0.1 \text{ mm/s}$  (from an applied stress up to  $120 \text{ MPa}$ ), we detected fronts moving at speeds between  $0.5$  and  $1.5 \text{ mm/s}$ . The cooling power showed values in the range of  $-2$  to  $-5 \text{ K/s}$ , reaching a maximum cooling power of  $-7 \text{ K/s}$  when the two fronts were merging. In the present flexocaloric experiments, driving the sample in the vertical direction at  $33 \text{ mm/s}$  (applying a vertical force of only  $8 \text{ N}$ ), we have found much faster front speeds, up to  $8 \text{ mm/s}$ . The cooling power reached a maximum value of  $-12 \text{ K/s}$ . Taking into account that only a fraction of the volume of the sample is transformed, the fact that we get higher cooling power must be attributed to the higher speed shown by the fronts. Large values of the speed of the transformation fronts relative to the vertical speed of the pins are also obtained in the simulations.

The dynamics of the fronts at the microscopic scale can be understood from the analysis of the AE signals. Their existence already demonstrates the role played by pinning effects in the advancement of the fronts. In experiments in which the structural transition is induced by changing temperature or by uniaxial stress,<sup>23</sup> the energy distribution (probability density) of the AE events is known to exhibit fat tails that can be characterized with a power-law exponent. The exponent of these power-laws is known to depend on the symmetry of the martensitic phase<sup>24</sup> and also on the driving mechanism.<sup>23</sup> In the present flexocaloric case, we do not obtain a fat tail distribution (power-law decay), but a log normal distribution. The observed difference can be attributed to the fact that the growing microstructure and the corresponding growth dynamics are highly constrained due to the strain gradients across the beam. Large transformation events are not allowed, thus decreasing the relative probability of very large avalanche events.

## VI. CONCLUSION

Our study has revealed that the flexocaloric effect in a three point bending experiment in superelastic materials involving a ferroelastic phase transition is a consequence of the movement of fronts separating untransformed regions from partially transformed

ones. These partially transformed regions display a fine microstructure combining different martensite variants and austenite domains, which adapts to the strain gradient across the beam.

The fact that the amount of the transformed sample is small has a direct relation to the total amount of heat exchanged. This is a serious drawback when comparing to the uniaxial elastocaloric case in which one is able to transform the full sample. On the other hand, flexocaloric mechanisms require very small vertical forces, which, in some devices, can be a clear advantage. Hysteresis is mainly controlled not by intrinsic nucleation barriers but by the existence of disorder in the sample that pins the advancement of the fronts. Nevertheless, in the three point bending geometry, one can achieve large front velocities that have a positive impact on the heating/cooling power.

In future studies, it would be very important to study the effect of the sample thickness and crystal orientation. This will influence the selection of the microstructure. If one could favor microstructures that adapt better to the strain gradient, one would increase the amount of transformed fraction. In addition, it would be interesting to study the influence of disorder (impurities, precipitates, vacancies) trying to favor larger avalanches and/or higher front speeds.

## ACKNOWLEDGMENTS

Financial support from Grant No. MCIN/AEI/10.13039/501100011033 (Spain) under Grant No. PID2020-113549RB-I00/AEI is acknowledged. The work of A.S. was supported by the U.S. Department of Energy.

## AUTHOR DECLARATIONS

### Conflict of Interest

The authors have no conflicts to disclose.

## Author Contributions

**Clàudia Pérez-Junyent:** Mechanical and IR measurements, data analysis and plots. **Marcel Porta:** Model, simulations, analysis, plots, writing, review and editing. **Emma Valdés:** AE measurements; data analysis and plots. **Lluís Mañosa:** sample preparation, measurements and review. **Antoni Planes:** conceptualization, model, writing, review and editing. **Avadh Saxena:** conceptualization and review. **Eduard Vives:** Mechanical, IR, and AE measurements, data analysis, plots, writing, review and editing.

**Clàudia Pérez-Junyent:** Formal analysis (equal); Investigation (equal); Visualization (equal). **Marcel Porta:** Data curation (equal); Formal analysis (equal); Investigation (equal); Methodology (equal); Software (equal); Validation (equal); Visualization (equal); Writing – original draft (equal); Writing – review & editing (equal). **Emma Valdés:** Formal analysis (equal); Investigation (equal); Visualization (equal). **Lluís Mañosa:** Conceptualization (equal); Funding acquisition (equal); Investigation (equal); Methodology (equal); Project administration (equal); Supervision (equal); Validation (equal); Writing – review & editing (equal). **Antoni Planes:** Conceptualization (equal); Investigation (equal); Methodology (equal);

Supervision (equal); Writing – original draft (equal); Writing – review & editing (equal). **Avadh Saxena:** Conceptualization (equal); Investigation (equal); Methodology (equal); Validation (equal); Writing – review & editing (equal). **Eduard Vives:** Funding acquisition (equal); Investigation (equal); Methodology (equal); Project administration (equal); Software (equal); Supervision (equal); Validation (equal); Visualization (equal); Writing – original draft (equal); Writing – review & editing (equal).

## DATA AVAILABILITY

The data that support the findings of this study are available from the corresponding author upon reasonable request.

## REFERENCES

- <sup>1</sup>R. Gauß, G. Homm, and O. Gutfleisch, “The resource basis of magnetic refrigeration,” *J. Ind. Ecol.* **21**, 1291–1300 (2017).
- <sup>2</sup>L. Mañosa and A. Planes, “Solid-state cooling by stress: A perspective,” *Appl. Phys. Lett.* **116**, 050501 (2020).
- <sup>3</sup>X. Moya and N. D. Mathur, “Caloric materials for cooling and heating,” *Science* **370**, 797–803 (2020).
- <sup>4</sup>E. Bonnot, R. Romero, L. Mañosa, E. Vives, and A. Planes, “Elastocaloric effect associated with the martensitic transition in shape-memory alloys,” *Phys. Rev. Lett.* **100**, 125901 (2008).
- <sup>5</sup>J. Tušek, K. Engelbrecht, R. Millán-Solsona, L. Mañosa, E. Vives, L. P. Mikkelsen, and N. E. Pryds, “The elastocaloric effect: A way to cool efficiently,” *Adv. Energy Mater.* **5**, 1500361 (2015).
- <sup>6</sup>L. Mañosa and A. Planes, “Materials with giant mechanocaloric effects: Cooling by strength,” *Adv. Mater.* **29**, 1603607 (2017).
- <sup>7</sup>M. Porta, T. Castán, A. Saxena, and A. Planes, “Flexocaloric effect near a ferroelastic transition,” *Phys. Rev. B* **104**, 094108 (2021).
- <sup>8</sup>R. Wang, S. Fang, Y. Xiao, E. Gao, N. Jiang, Y. Li, L. Mou, Y. Shen, W. Zhao, S. Li, A. F. Fonseca, D. S. Galvão, M. Chen, W. He, K. Yu, H. Lu, X. Wang, D. Qian, A. E. Aliev, N. Li, C. S. Haines, Z. Liu, J. Mu, Z. Wang, S. Yin, M. D. Lima, B. An, X. Zhou, Z. Liu, and R. H. Baughman, “Torsional refrigeration by twisted, coiled, and supercoiled fibers,” *Science* **366**, 216 (2019).
- <sup>9</sup>A. Czernuszewicz, L. Griffith, J. Slaughter, and V. Pecharsky, “Low-force compressive and tensile actuation for elastocaloric heat pumps,” *Appl. Mater. Today* **19**, 100557 (2020).
- <sup>10</sup>D. J. Sharar, J. Radice, R. Warzoha, B. Hanrahan, and A. Smith, “Low-force elastocaloric refrigeration via bending,” *Appl. Phys. Lett.* **118**, 184103 (2021).
- <sup>11</sup>R. Wang, X. Zhou, W. Wang, and Z. Liu, “Twist-based cooling of polyvinylidene difluoride for mechanothermochromic fibers,” *Chem. Eng. J.* **417**, 128060 (2021).
- <sup>12</sup>H. Hou, S. Qian, and I. Takeuchi, “Materials, physics and systems for multicaloric cooling,” *Nat. Rev. Mater.* **7**, 633 (2022).
- <sup>13</sup>P. Chowdhury, “Frontiers of theoretical research on shape memory alloys: A general overview,” *Shape Mem. Superelasticity* **4**, 26–40 (2018).
- <sup>14</sup>E. Bonnot, E. Vives, L. Mañosa, A. Planes, and R. Romero, “Acoustic emission and energy dissipation during front propagation in a stress-driven martensitic transition,” *Phys. Rev. B* **78**, 094104 (2008).
- <sup>15</sup>A. Planes, L. Mañosa, and E. Vives, “Acoustic emission in martensitic transformations,” *J. Alloys Compd.* **577**, S699–S704 (2013).
- <sup>16</sup>R. Niemann, J. Kopeček, O. Heczko, J. Romberg, L. Schultz, S. Fähler, E. Vives, L. Mañosa, and A. Planes, “Localizing sources of acoustic emission during the martensitic transformation,” *Phys. Rev. B* **89**, 214118 (2014).
- <sup>17</sup>P. Howell, G. Kozyreff, and J. Ockendon, *Applied Solid Mechanics* (Cambridge University Press, 2009).

- <sup>18</sup>S. Kartha, J. A. Krumhansl, J. P. Sethna, and L. K. Wickham, "Disorder-driven pretransitional tweed pattern in martensitic transformations," *Phys. Rev. B* **52**, 803–822 (1995).
- <sup>19</sup>L. Ianniciello, M. Romanini, L. Mañosa, A. Planes, K. Engelbrecht, and E. Vives, "Tracking the dynamics of power sources and sinks during the martensitic transformation of a Cu–Al–Ni single crystal," *Appl. Phys. Lett.* **116**, 183901 (2020).
- <sup>20</sup>G. Capellera, L. Ianniciello, M. Romanini, and E. Vives, "Heat sink avalanche dynamics in elastocaloric Cu–Al–Ni single crystal detected by infrared calorimetry and Gaussian filtering," *Appl. Phys. Lett.* **119**, 151905 (2021).
- <sup>21</sup>E. Vives, D. Soto-Parra, L. Mañosa, R. Romero, and A. Planes, "Imaging the dynamics of martensitic transitions using acoustic emission," *Phys. Rev. B* **84**, 060101(R) (2011).
- <sup>22</sup>A. Planes and E. Vives, "Avalanche criticality in thermal-driven martensitic transitions: The asymmetry of the forward and reverse transitions in shape-memory materials," *J. Phys.: Condens. Matter* **29**, 334001 (2017).
- <sup>23</sup>E. Vives, D. Soto-Parra, L. Mañosa, R. Romero, and A. Planes, "Driving-induced crossover in the avalanche criticality of martensitic transitions," *Phys. Rev. B* **80**, 180101(R) (2009).
- <sup>24</sup>L. Carrillo, L. Mañosa, J. Ortín, A. Planes, and E. Vives, "Experimental evidence for universality of acoustic emission avalanche distributions during structural transitions," *Phys. Rev. Lett.* **81**, 1889 (1998).